JGR Solid Earth

RESEARCH ARTICLE
10.1029/2019JB017584

The Latest Spreading Periods of the South China Sea: New Constraints From Macrostructure Analysis of IODP Expedition 349 Cores and Geophysical Data

Zhen Sun[1,2], Weiwei Ding[3], Xixi Zhao[4], Ning Qiu[1,2], Jian Lin[1,2,5], and Chun-Feng Li[6]

[1]CAS Key Laboratory of Ocean and Marginal Sea Geology, South China Sea Institute of Oceanology, Guangzhou, China, [2]Innovation Academy of South China Sea Ecology and Environmental Engineering, Chinese Academy of Sciences, Guangzhou, China, [3]Second Institute of Oceanography, Ministry of Natural Resources, Hangzhou, China, [4]State Key Laboratory of Marine Geology, Tongji University, Shanghai, China, [5]Department of Geology and Geophysics, Woods Hole Oceanographic Institution, Woods Hole, MA, USA, [6]Ocean College, Zhejiang University, Zhoushan, China

Abstract Macrostructures preserved in deformed rocks are essential for the understanding of their evolution, especially when the deformation is weak and hard to discriminate in regional scale or purely through geophysical data. In order to resolve the inconsistency between NS trending fracture zones and NE oriented spreading fabrics of the South China Sea during the latest spreading stage, we analyzed macrostructures identifiable from the basalt and consolidated sediment samples of the Integrated Ocean Drilling Program (IODP) Sites U1431 and U1433. These two sites are close to the East and Southwest relict spreading ridges and provide critical information on the latest spreading stages. The structures in the basalt of both sites suggest two dominant orientations of NS and NE. At U1431, sediments show mainly WNW trending slickensides, different from that of basalt. At U1433, no structures were found in postspreading sediment. Thus, NE and NS trending structures in basalt are most possibly formed by seafloor spreading. Crosscutting relationship suggests that NE trending structures formed first, followed by NS and finally WNW trending structures. These observations are consistent with geophysical features. Magnetic anomalies and ocean bottom seismometer velocity suggest that the latest relict ridge of the East Subbasin coincides with the EW trending seamount chain. Located between the relict ridges of East and Southwest Subbasins, NS trending Zhongnan-Liyue Fracture Zone had acted as the latest transform fault. Based on the above evidences, we proposed that the South China Sea may have experienced a short period of NS oriented spreading after earlier SE spreading. These results resolve the previous inconsistencies.

Key Points:
- Basalt and sediment show different macrostructure orientations, indicating different stress fields between the synspreading and postspreading stages
- Magnetic anomalies and low upper crust *P* wave velocities indicate that the youngest relict ridge in the East Subbasin may coincide with a seamount chain
- Cross-cutting relationship of fractures suggests a short period of roughly NS trending spreading after a SE trending spreading

Supporting Information:
- Supporting Information S1

Correspondence to:
W. Ding, Z. Sun, and X. Zhao,
wwding@sio.org.cn;
zhensun@scsio.ac.cn;
xzhao@tongji.edu.cn

Citation:
Sun, Z., Ding, W., Zhao, X., Qiu, N., Lin, J., & Li, C.-F. (2019). The latest spreading periods of the South China Sea: New constraints from macrostructure analysis of IODP Expedition 349 cores and geophysical data. *Journal of Geophysical Research: Solid Earth*, *124*, 9980−9998. https://doi.org/10.1029/2019JB017584

Received 22 FEB 2019
Accepted 20 AUG 2019
Accepted article online 29 AUG 2019
Published online 14 OCT 2019

©2019. American Geophysical Union. All Rights Reserved.

1. Introduction

Deformed rocks are one of the few direct sources of information available for the reconstruction of tectonic evolution. Successive stages in the deformational and metamorphic evolution of a rock are commonly preserved as part of a fabric. The recognition and correct interpretation of these fabrics is essential for the understanding of their evolution, especially when the deformation is weak and hard to discriminate in regional scale or purely through geophysical data.

The South China Sea (SCS) is one of the largest marginal seas in the west Pacific (Figure 1). Surrounded by the Eurasia, Indo-Australia, and Pacific plates, SCS holds important tectonic evidence for Southeast Asia. Existing data suggest that the rifting and spreading direction of the SCS has changed frequently. With up to 2,000 m of sediment cover and complex postspreading volcanism, the age and the spreading history of the SCS basin have long been controversial (Barckhausen et al., 2014; Briais et al., 1993; Morley, 2002, 2012; Sun et al., 2006, 2009; Yao et al., 1994). Previous researches show some discrepancy toward the location of the East Subbasin's relict ridge (ERR) and the Zhongnan-Liyue fault zone (ZFZ) but no controversy toward the spreading direction of the last spreading stage. However, the SE oriented spreading direction is oblique to the NS trending fracture zone. In both bathymetry (Figure 1) and the new gravity anomaly map (Hwang & Chang, 2014), NS trending fractures and seamount chains connecting or locating between ERR and SW Subbasin's relict ridge (SWRR) are observed. Sibuet et al. (2016) attributed these NS trending structures to postspreading NS extension, but no evidence support such a stress field. The postspreading faults (active from about 16 to 5.3 Ma) in the northern continental margin trend mainly WNW and nearly EW and

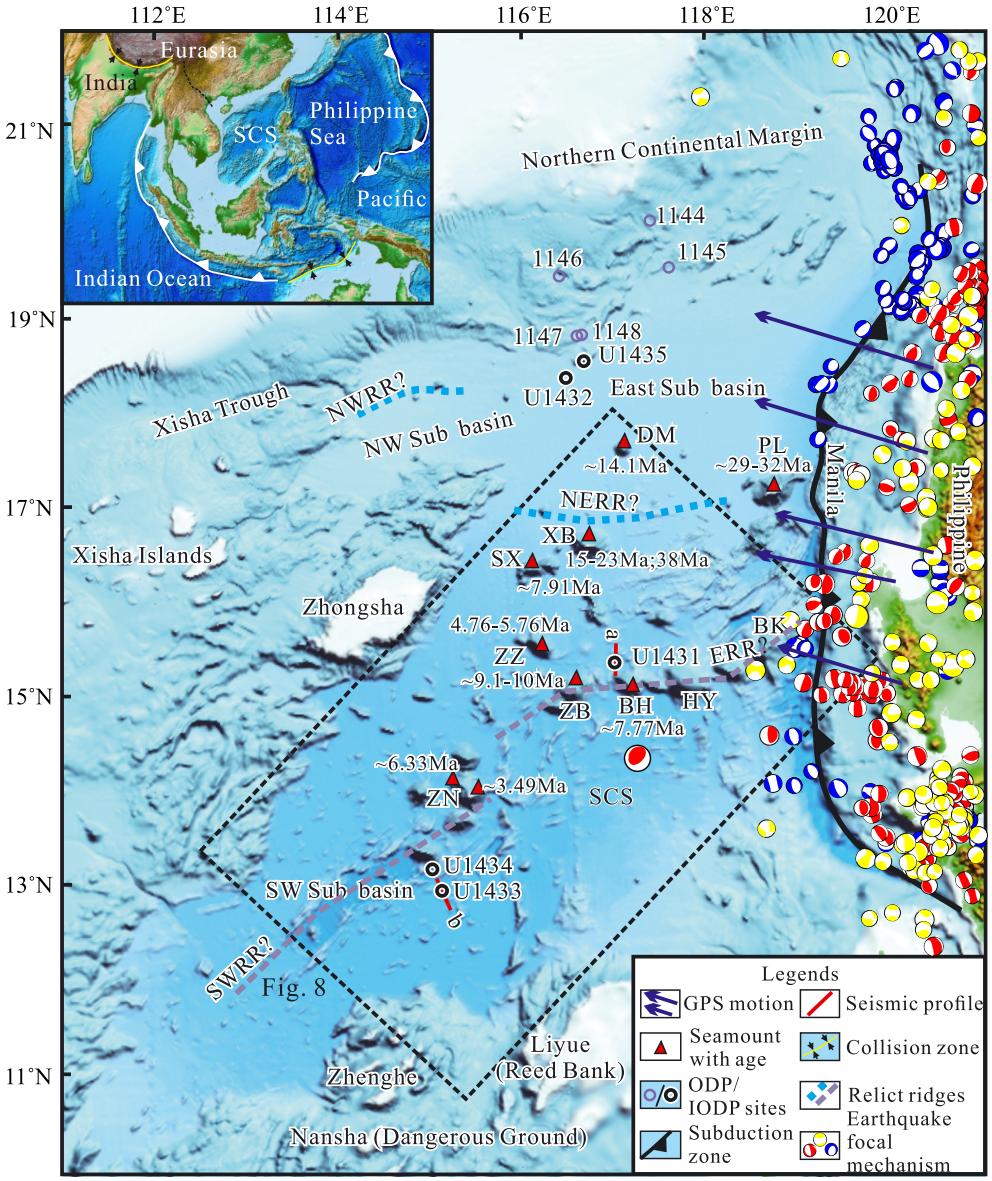

Figure 1. Regional structure map of the South China Sea basin. The bathymetry basemap is courtesy of Guangzhou Marine Geological Survey. The ages of the dredge samples were indicated around the seamounts (Li et al., 1991; Tu et al., 1992; Wang et al., 2009; Yan et al., 2008; Yang et al., 2011; Zhong et al., 2018). Plate motion measured by several GPS stations is referenced from Yu and Kuo (1999). Earthquake focal mechanism is plotted with Harvard (1976–2010) data; blue balls mean normal fault earthquake, red balls indicate thrust fault earthquake, and yellow balls suggest strike-slip fault earthquake. NWRR = Northwestern Relict Ridge; NERR = Northeastern Relict Ridge; SWRR = Southwestern Relict Ridge; ERR = Eastern Relict Ridge; IODP = Integrated Ocean Drilling Program. The abbreviations and markers have the same meaning in the following figures.

suggest a WNW compression (Li, 1989; Sun et al., 2014; Xie et al., 2017), similar to the present-day stress field deduced from GPS (Yu & Kuo, 1999).

In order to resolve the above-mentioned inconsistencies, we analyzed the macrostructures (about 300 fractures, veins, and slickensides) in core samples from the Integrated Ocean Drilling Program (IODP) Expedition 349 to provide an independent evidence. However, first-hand macrostructural analysis of IODP core samples had seldom been published, because the limited size of core samples makes it difficult to obtain a full view of the regional structure or large-scale tectonics. On the other hand, there will be a certain degree of error (up to 10–20%) in the measurement and correction of the macrostructures. In order to ensure the

accuracy of the macrostructure analysis, all the available geophysical data in this area were utilized to jointly constrain the analysis. Therefore, we measured and corrected most visible fractures, veins, and slickensides first. Then, we divided these structures into different groups according to their locations, ages, or dip angles to determine their plane directions in different stages. Finally, we integrate these results with seismic, topographic, gravity, magnetic, and also *P* wave velocity data to interpret the history of the regional deformation. This study will exemplify how the kinematics of sea basin evolution can be synthesized from macroscale structures and larger-scale geophysical data.

2. Geological Background

SCS has a rhomb-shaped oceanic basin, wide in the east and narrow in the west. Based on interpretation of magnetic anomalies, Taylor and Hayes (1980, 1983) suggested that the East Subbasin opened in a roughly NS direction from about 32 to 17 Ma. The relict ridge (inactive spreading center) locates roughly along the EW trending seamount chain, where magma was supposed to erupt along thinned oceanic lithosphere under postspreading stress field. Briais et al. (1993) estimated the spreading age of the Southwest (SW) Subbasin to be from about 23 to 16 Ma based on compilation and interpretation of additional magnetic anomaly data and proposed that the SCS started spreading in the east and propagated to the southwest after about 25 Ma.

Pautot et al. (1986) and Briais et al. (1993) use multibeam bathymetric data to suggest that both the East and SW Subbasin should have opened in a NW-SE direction during the Early to Middle Miocene. The ERR is ENE trending and was dissected by large amounts of NW trending transform faults to keep each segment trending NE. Using a similar data set, Yao et al. (1994) suggested that the SW Subbasin may have opened from 42 to 35 Ma, and it is separated from the East Subbasin by a NS trending ZFZ. Yao et al.'s (1994) model appeared to be inconsistent with the breakup unconformity in the northern continental margin, which developed early in the east and late in the west (Hutchison, 2014; Ru, 1988; Sun et al., 2011; Zhou et al., 1995). Integrated with high-resolution bathymetry, Barckhausen et al. (2014) suggested a similar position for the relict ridge as Briais et al. (1993), and he also suggested that the relict ridge was crosscut by several NW trending fracture zones. They showed a curved ZFZ composed of several segments, with the central youngest one trending roughly NS. Li et al. (2014) suggested a 31–16 Ma spreading duration, and a similar relict ridge position as Barckhausen et al. (2014), but a NS trending ZFZ as Yao et al. (1994).

IODP Expedition 349 carried out from February to April 2014 proved that the Oligocene to Miocene spreading duration is most reasonable (Li, Lin, et al., 2015). A total of 1,602 m cores was recovered from five drill sites in the deep basin of the SCS (Li, Lin, et al., 2015). Site U1431 is located close to ERR, Sites U1433 and U1434 are located close to the SWRR, and Sites U1432 and U1435 are close to the northern ocean boundary, respectively (Figure 1). Radiometric dating indicates that the SCS stopped spreading at about 15 Ma (Koppers, 2014), with slightly younger ages for the East Subbasin than for the SW Subbasin (Figure 2). Dating also suggested that postspreading volcanic activity near Site U1431 (with geochemical signatures similar to those of oceanic island basalt) started to be active at about 6 to 8 Myr after seafloor spreading terminated (Koppers, 2014; Li, Lin, et al., 2015), which agrees well with dredging results from the seamounts (Figure 1; Yan et al., 2008; Yang et al., 2011).

Sibuet et al. (2016) reevaluated the spreading history of the SCS based on detailed analysis of more recent geophysical data and newly reported radiometric ages of oceanic basalt. They proposed that the ERR may deviate from the postspreading volcanic chain and trend at N55°; by this way the ridge orientation is consistent with the spreading fabrics and magnetic anomalies in the neighboring area.

3. Data and Methods

In this study, core samples, seismic profiles, multibeam bathymetry, free-air anomalies (FAAs) of gravity (Sandwell et al., 2014), magnetic anomaly data (Ishihara & Kisimoto, 1996), *P* wave velocity (Zhang et al., 2016; He et al., 2016), and earthquake focal mechanisms were used.

3.1. Structural Orientation Measurement and Correction

Both basalt and consolidated sedimentary cores were used for macrostructure measurement at Sites U1431 and U1433. The first step is to discriminate real structures from pesudostructures caused by drilling

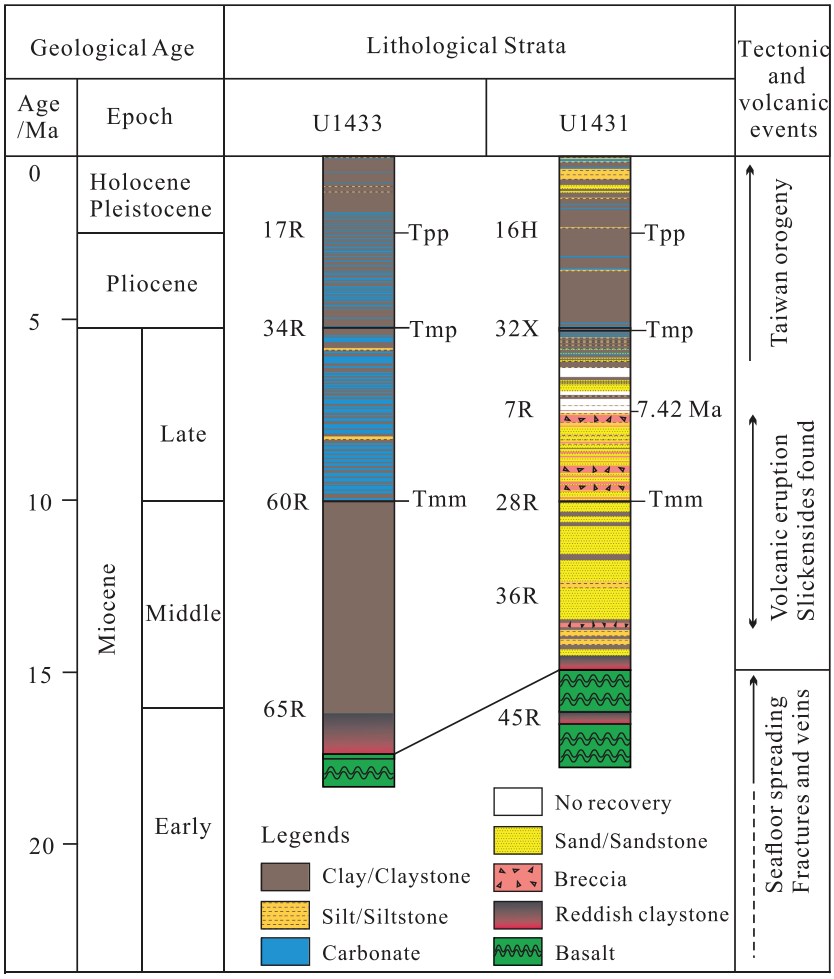

Figure 2. Stratigraphic column of Sites U1431 and U1433; the lithology and age information are according to Li, Lin, et al. (2015). For sequence boundaries, Tpp = Pliocene-Pleistocene boundary; Tmp = Miocene-Pliocene boundary; Tmm = middle Miocene-late Miocene boundary.

operation. Often, the core will break along preexisting fractures or veins. It is easy to distinguish real fractures from induced fractures based on color and secondary minerals on the fault plane. Highly sinuous or irregular structures are not measured for orientation distribution.

Archived halves were mainly used for structural measurements. However, planes with slickensides were estimated from the working halves. Our techniques generally followed Harris et al. (2013). The detailed procedure was described in the supporting information and the IODP proceedings (Kinoshita et al., 2009; Li, Lin, et al., 2015; Vannucchi et al., 2012).

Due to drilling-induced rotation of each core segment, the extended core barrel and rotary core barrel intervals require paleomagnetic reorientation, so that the real dip angle and dip direction in the geographic reference frame can be obtained. However, the inaccurate estimate of dip angles by using limited measuring tools may cause up to several degrees of deviation to the dip direction and dip angle, especially for very steep or very gentle structures. The paleomagnetic measurement also affects the accuracy of the structural orientation estimates. We estimated that up to 10–20% of error might be caused by the measuring and correcting procedure.

In this paper, 22 planes with slickensides were measured for postspreading sediment, so the corresponding analysis was less reliable than those of the veins and fractures, of which about 130 measurements at Site U1431 and about 140 measurements at Site U1433 were obtained.

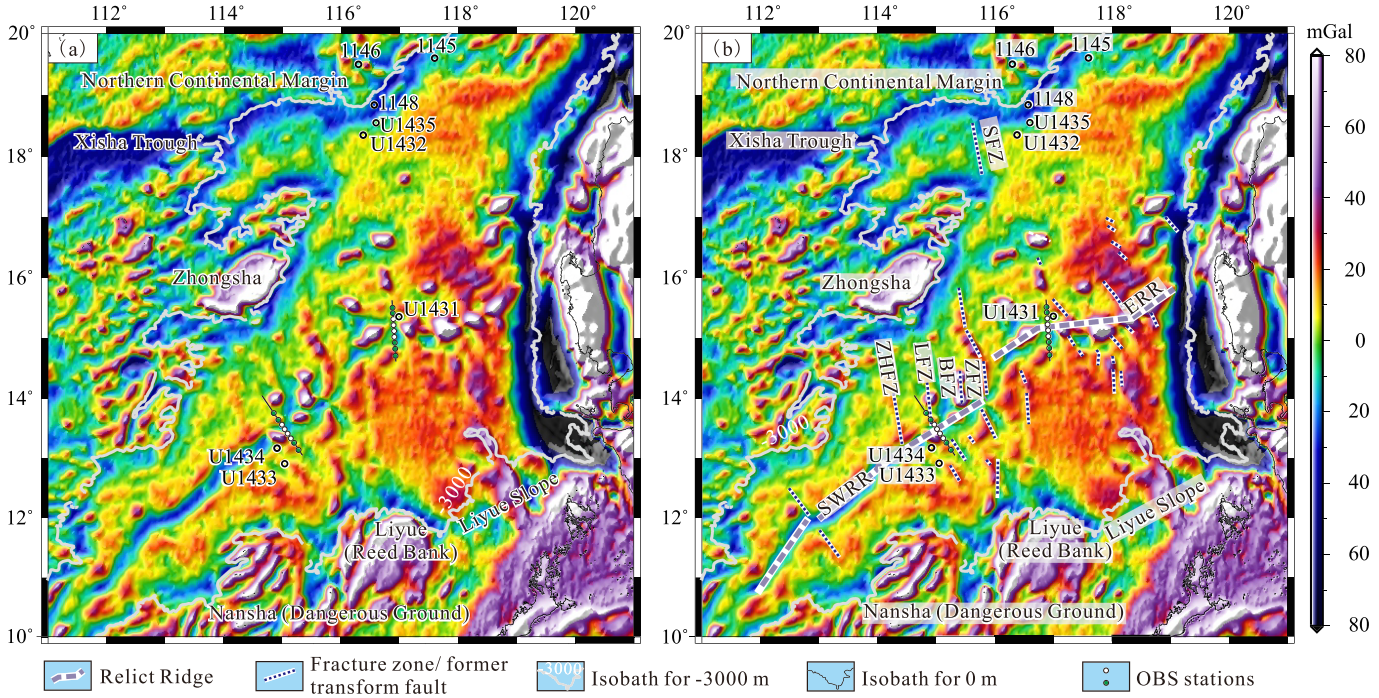

Figure 3. Original (a) and interpreted (b) Free Air Gravity Anomaly map of the South China Sea basin. Blue dotted lines with white background are conjectured fracture zones interpreted based on bathymetry (Figure 1) and free air gravity. SW Subbasin's relict ridge and nearly NS trending, NW trending fracture zones are discriminated, while East Subbasin's relict ridge is not confirmed with confidence. ZFZ = Zhongnan-Liyue fault zone; SFZ = Shenhu-Yitongansha fault zone; BFZ = Beiyue-Nanyue fault zone; LFZ = Longnan fault zone; ZHFZ = Zhenghe fault zone. The abbreviations and markers have the same meaning in the following figures.

3.2. Geophysical Data

The FAA map (Figure 3) was generated from the global gravity model (V23) of Sandwell et al. (2014), which has a resolution of 30 arc sec. The principle of using gravity anomalies to identify large structures such as relict ridges was described by Watts (2001). He proposed from gravity anomaly and topographic data that oceanic rifts have a certain flexural strength despite high temperatures. Even at ridges that ceased spreading more than 40 to 60 Ma, such as in the Labrador Sea and the Coral Sea, FAAs present similar features to those active rifts (Watts, 2001). When a relict ridge is covered by thick sediments and cannot be discerned through bathymetry, FAAs can help significantly in discriminating the relict ridge in plan view (Sandwell et al., 2014).

The magnetic anomaly map (Figure 4) was generated using the 1-arc min data set of East and Southeast Asia, which was compiled from available shipboard and some onland magnetic data by the Geological Survey of Japan and the Coordinating Committee for Coastal and Offshore Geoscience Programs in East and Southeast Asia (Ishihara & Kisimoto, 1996). Magnetic anomalies in the oceanic crust can help to identify the spreading direction, especially in areas with thick sediments or late volcanism, where spreading fabrics were covered.

Earthquake focal mechanisms are used to identify active tectonic events. In this paper, we used data from Harvard (1976–2010; Dziewonski et al., 1981; Ekström et al., 2012). The data suggest that south of U1431, a thrust earthquake (M_w = 5.3) occurred in 1998, which indicates that the fault (with plane trending NE) may still be active (Figure 1).

3.3. Seismic Profiles

Seismic data across the drill sites were obtained from two different surveys. Lines named “nds” were collected by the Second Institute of Oceanography (~6,237.5 m, 480 channels, and 2,400 m, 48 channels, respectively). Lines named 973 were collected by the South China Sea Institute of Oceanology with relatively short streamers (~3,000 m, 48 channels). The primary processing flow for these data included multiple attenuation

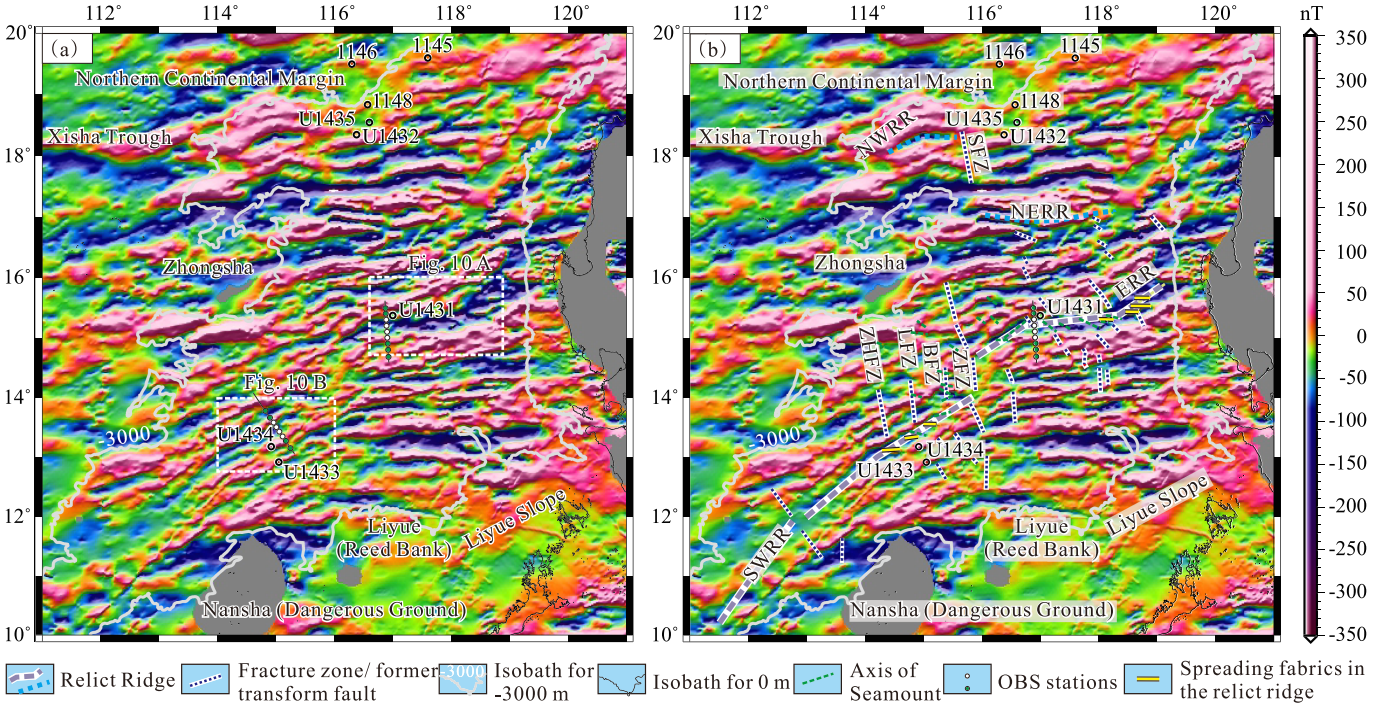

Figure 4. Original (a) and interpreted (b) magnetic anomaly map of the South China Sea basin. The magnetic anomaly data are from Ishihara and Kisimoto (1996). The map was drawn with a Mercator projection and 1-arc min grid spacing. Blue dotted lines with white background are conjectured fracture zones interpreted based on bathymetry (Figure 1) and free air gravity (Figure 3). Blue and lilac dashed lines are conjectured relict ridges interpreted mainly according to magnetic anomaly constrained by lineations discriminated by Briais et al. (1993) and Li et al. (2014).

and prestack time migration. Seismic interpretation was carried out through ties with the drill sites; the age of sequence boundaries are dated with microfossils of IODP drill sites (Li, Lin, et al., 2015; Li, Li, et al., 2015).

4. Results

4.1. Structures at Site U1431 in the East Subbasin

Site U1431 is located at about 15 km north of the volcanic chain (Figure 1) and about 200 km west of the Manila subduction zone. According to the bathymetric map of Guangzhou Marine Geological Survey (Figure 1), and the interpretation of Barckhausen et al. (2014), Site U1431 is close to a NW trending (~N310°) fracture zone. South of the ERR, more NW oriented fracture zones are present on the seafloor.

In seismic profile across Site U1431 (Figure 5a), many faults with several to tens of meters of vertical offset developed in the postspreading sequences, especially before 7.42 Ma. Most of them are normal faults, but two are apparently thrust faults (f1 and f2 in Figure 5a). Thrusting movement occurred close to the fracture zone, around and after middle Miocene (Tmm ~10 Ma). The fracture zone also showed clear vertical offset (>150 m) at around 7.42 Ma in profile 973SCSIO01e (Figure 5a). Beneath the sedimentary sequences, a strong reflection boundary Tg marks the top of the igneous basement where basalt was recovered. Within the basement, layered reflections cut by small faults could be identified for at least 200 ms thick in two-way travel time, thicker below the sag center than in the slope area (Figure 5a). According to the drilling results, layered reflections may be caused by periodic basalt eruption interlayered with reddish claystone.

Fractures, veins, and slickensides were mainly found and measured in the intermediate to completely consolidated sediments older than 7.42 Ma (sequence SL in Figure 5a), and mainly in claystone and siltstone. In more rigid and consolidated volcaniclastic cores, structures are absent, but angular contact relationships between sequences were occasionally observed (Figure 6a). In reddish claystone, both displaced clay clasts and angular contact relationship between different sequences were observed (Figure 6b). In basalt cores, veins and fractures were often observed (Figures 6c–6f). Partial veins were arched or even sinuous (Li, Lin, et al., 2015), and some veins combined to appear radial or concentric in shape, parallel to the cooling

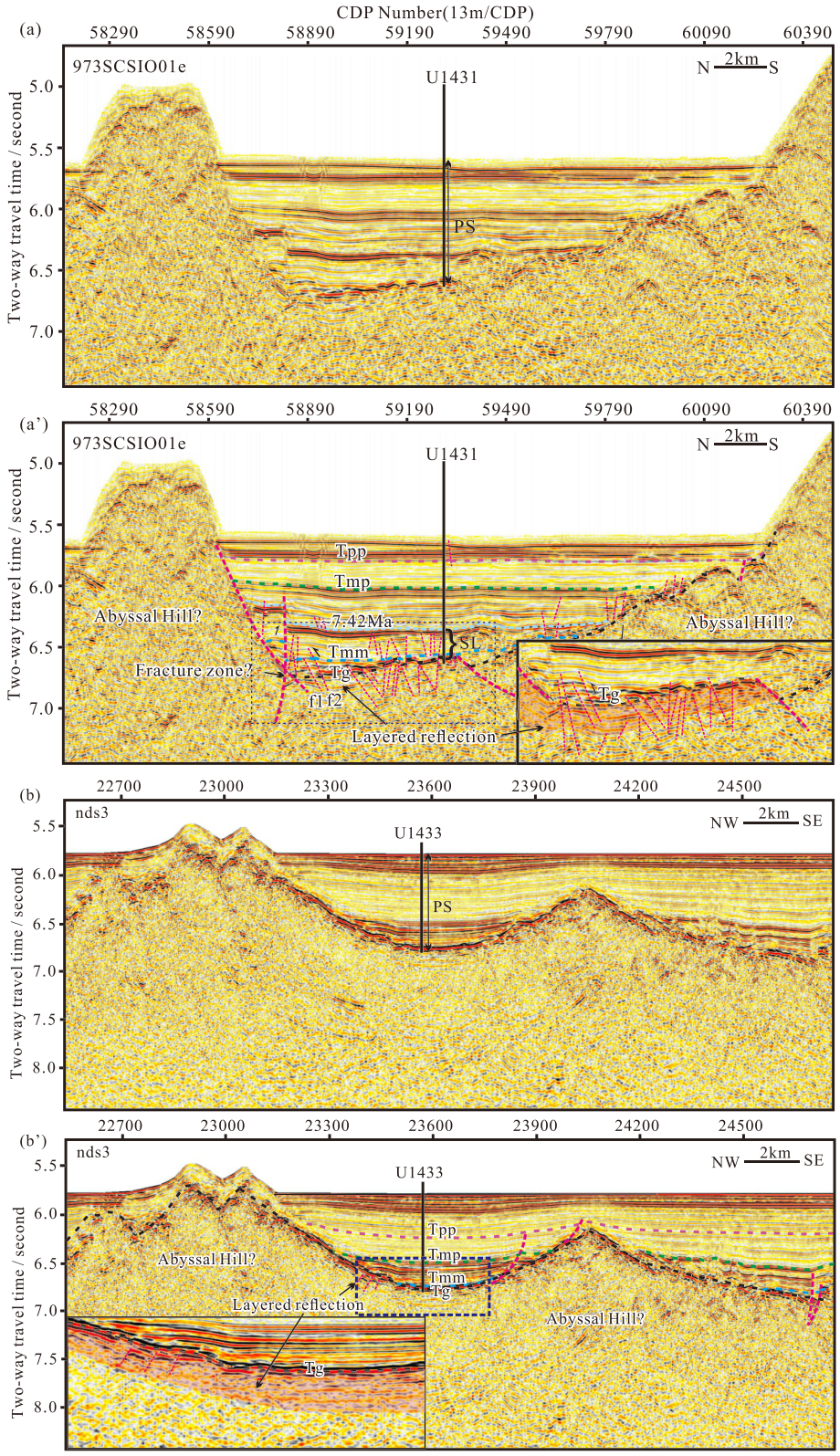

Figure 5. Original and interpreted seismic profiles across the drill Sites U1431 (a and a′) and U1433 (b and b′). The names for the sequence boundaries are after Li, Li, et al. (2015). SL indicates sedimentary succession that slickensides were found. PS means postspreading sediment. The positions of the seismic lines are shown in Figure 1 as a and b. Tpp = Pliocene-Pleistocene boundary; Tmp = Miocene-Pliocene boundary; Tmm = middle Miocene-late Miocene boundary.

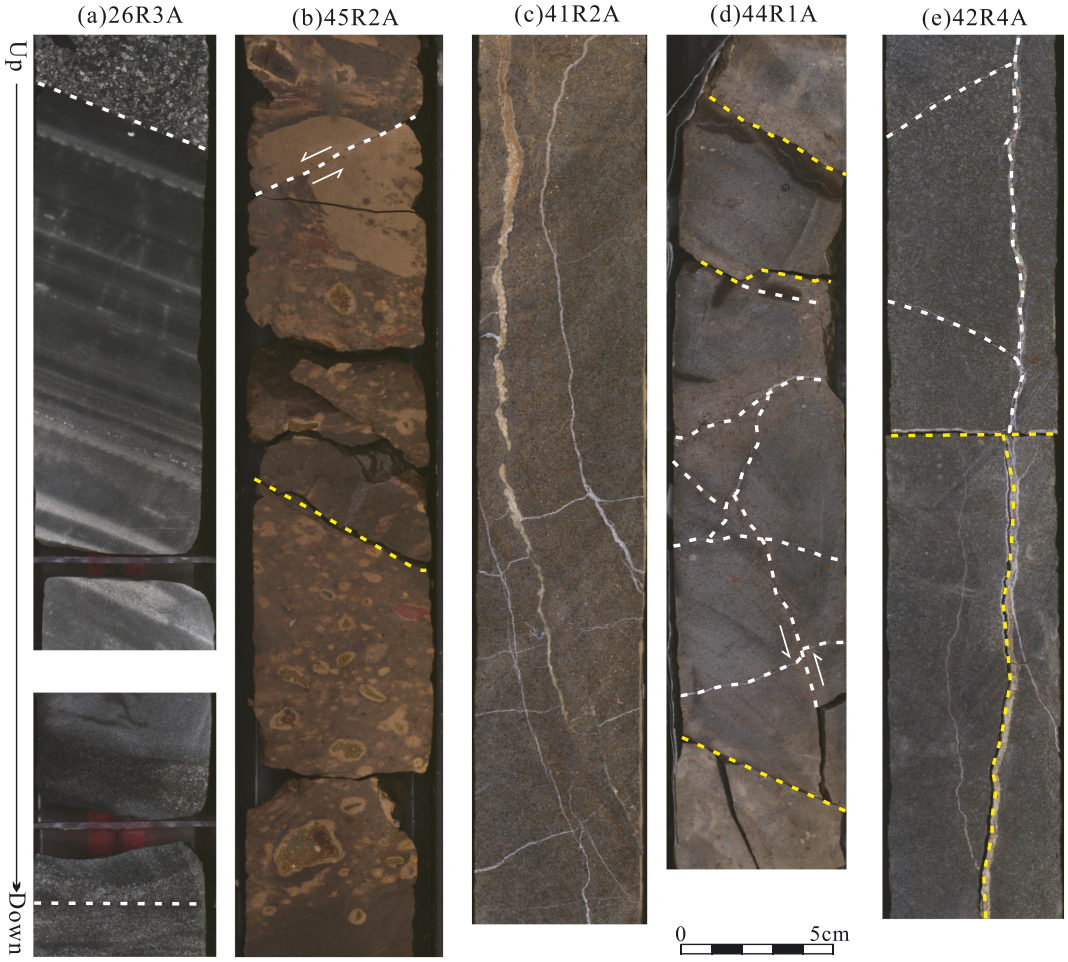

Figure 6. Core samples at Site U1431 with offset, fractures, and veins. White dashed lines are veins or sequence boundaries between layers with different dipping angles. Yellow dashed lines are fractures. These symbols have the same meaning in Figures 7 and 9. (a) No fault or fracture was found in volcanic clastic sequence, but there is a segment of sediment which has different sequence dipping angles and lithological composition between two relatively horizontal sediment layers. (b) In reddish claystone, a muddy clast was displaced. There are two other conjectured boundaries with quite different lithological compositions from beneath and above. (c) In some pillow basalts, concentric and radial veins could be seen. (d) In some other pillow basalts, both arched and straight veins could be seen. (e) In the massive flow basalt, straight veins or fractures are more overwhelming. Question marks mean uncertainty about its joint relationship. White arrows indicate the conjectured movement along the fracture or fault.

fringe or pointing from the rock center toward the surface, likely to be related with the cooling of magma (Figure 6c). Fractures are largely straight in the pillow basalt and the massive flow basalt (Figures 6e and 6f).

Slickensides were found both in the postspreading sediment cores and the reddish claystone between two stages of synspreading basalt. According to the step direction, slickensides in sediment samples appear mostly normal movement but with few thrusting (Figure 7b). This finding is also consistent with seismic interpretations (Figure 5a′). However, slickensides in reddish claystone between two stages of basalt are nearly horizontal, suggesting mainly horizontal shearing movement. Typically, the slickensides appear more slippery and shiny than the other parts of the cores (Figures 6b–6e). The youngest sequence in which slickensides were found was about 7.42 Ma in age. This age is also consistent with the seismic profile, which show that the faults generally ceased activity after 7.42 Ma. Only few faults can keep active until 5.3 Ma (Figure 5a′). When zoomed in 80 times under a microscope, small crystal bunches could be seen linearly arranged along the planes (Figure 7f), suggesting that the planes with slickensides are old structures and should not be drilling induced.

Measurements on strike distribution indicate that veins and fractures in basalt show preferential orientations in roughly NE (N50–60°) and NS (N350–360°) directions (Figure 8a1). The secondary preferential orientations are nearly EW (N90–100°E) and WNW (N290–300°). The dip angles vary in a wide range from

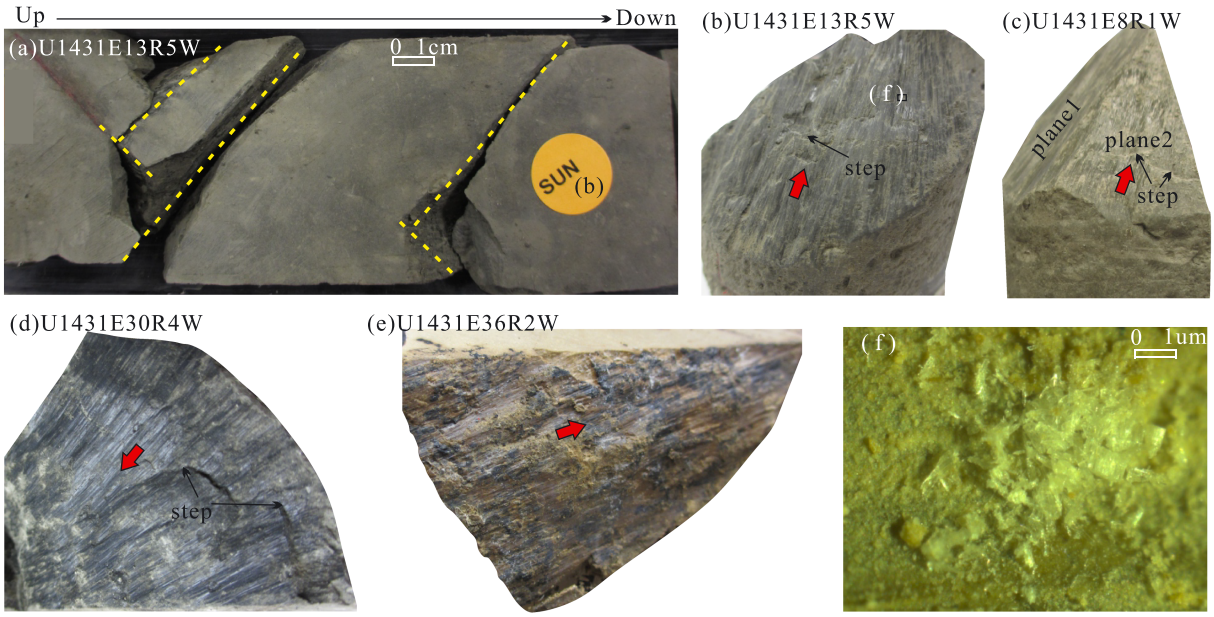

Figure 7. Photos for structural planes with slickensides in core samples (a–e) and under microscope (f) at Site U1431. Red arrows indicate the moving direction of the contrary plate judged from steps. (a) Intermediate consolidated sediment cores with conjugate fractures and slickensides were found on the fracture planes. (b–d) Slickensides on the core samples. (e) Slickensides in reddish claystone between two basalt layers. (f) Small bunches of crystals can be observed under the microscope, which grow in line along slickensides. Yellow dashed lines are fractures.

0° to 90° (Figure 8c1). NE, EW, and WNW trending structures dip slower than 60° (Figure 8a2), while roughly NS and NNW trending (N320–330°) structures show steep dip angles of 60–90°, suggesting that they might be strike-slip faults (Figure 8a3). These two sets of structures are perpendicular to the EW and NE trending structures. The lower basalt layer is dominated by NE and NNW trending fault pairs (Figure 8a4), and with secondary pairs trending NS and EW. The upper basalt layer shows almost equally strong distributions in NE, EW, NS, and NW trending faults (Figure 8a5), which suggests that the stress field may have changed from the lower basalt layer to the upper one.

Planes with slickensides in postspreading sediments show three prevailing directions (Figure 8a6), the most dominant is WNW (N300–310°), followed by roughly EW (N80–90°) and NNE (N20–30°). The dip angles are mainly 45–72° (Figure 8c2). The postspreading sediments show completely different structure orientations from the basalt, suggesting that they might be fractured by different stress field or tectonic events.

4.2. Structures at Site U1433 in the Southwest Subbasin

Site U1433 is located at about 30 km southeast of the relict ridge (SWRR). The rift valley along the ridge is about 30 km wide (Ding et al., 2013, 2016; Li et al., 2012). Based on interpretation of magnetic anomaly data, the spreading rate of the Southwest Subbasin is about 20–40 mm/year (Briais et al., 1993; Li et al., 2014), which makes it a slow-spreading basin. The fracture zones near U1433 trend about N315° (Figure 3).

Compared with Site U1431, fewer faults are present near this drill site in the seismic profile (Figure 5b and 5b′), and the sedimentary sequences appear horizontally continuous and parallel. The basement below the postrifting sediments (below Tg) also shows very clear interlayered reflection for about 200 ms in two-way travel time. This interlayered reflection also thins toward the sag slope. However, no interlayered reddish claystone was drilled, possibly because only ~60 m of basalt was penetrated in 1433. Interlayered reddish claystone was encountered at ~72 m below the basement of U1431.

In intermediate to completely consolidated sediment samples, very few structures were found. Most of the structures are irregular in shape and subparallel to bedding and are conjectured to be contraction cracks (Figure 9a) caused by loss of pore water or decompressive expansion after subaerial exposure. There are also several drilling induced cracks which have very fresh fracture planes. Fractures in sediments were not counted nor measured.

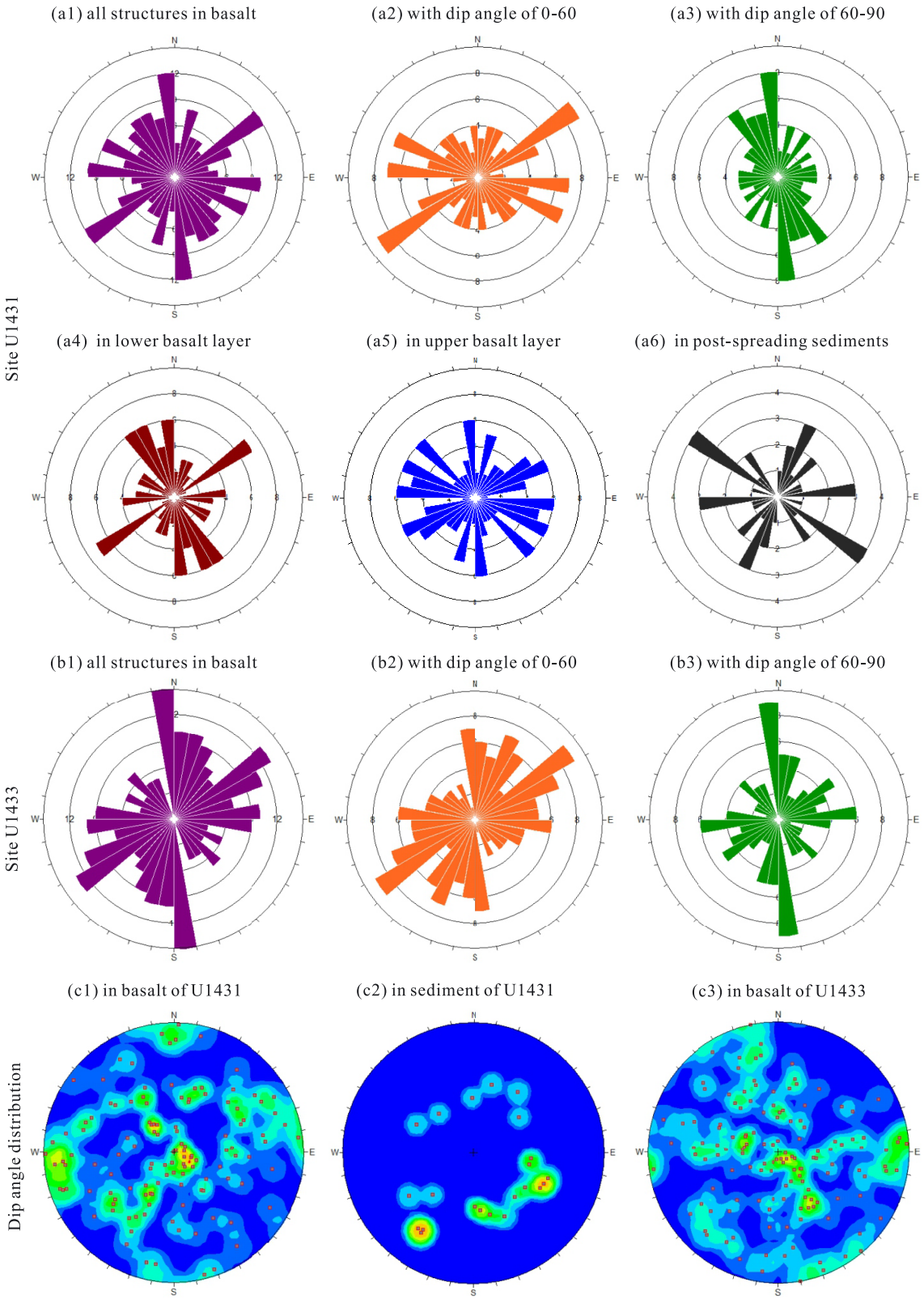

Figure 8. Orientation distribution of structures at Site U1431 (a1–a6) and Site U1433 (b1–b3) as well as their dip angle distribution (c1–c3). (a1, c1) and (b1, c3) are the strike and dip angle distribution rosette maps for all structures at Sites U1431 and U1433. (a2, b2) and (a3, b3) are strike distribution rosette maps for structures with dip angle of 0–60° and 60–90°. a4 and a5 are strike distribution for structures in the lower and upper basalt layer. a6 and c2 indicate the strike and dip angle distribution of planes with slickenside in postspreading sediment. The lower hemisphere equal angle projection was used in dip angle distribution maps.

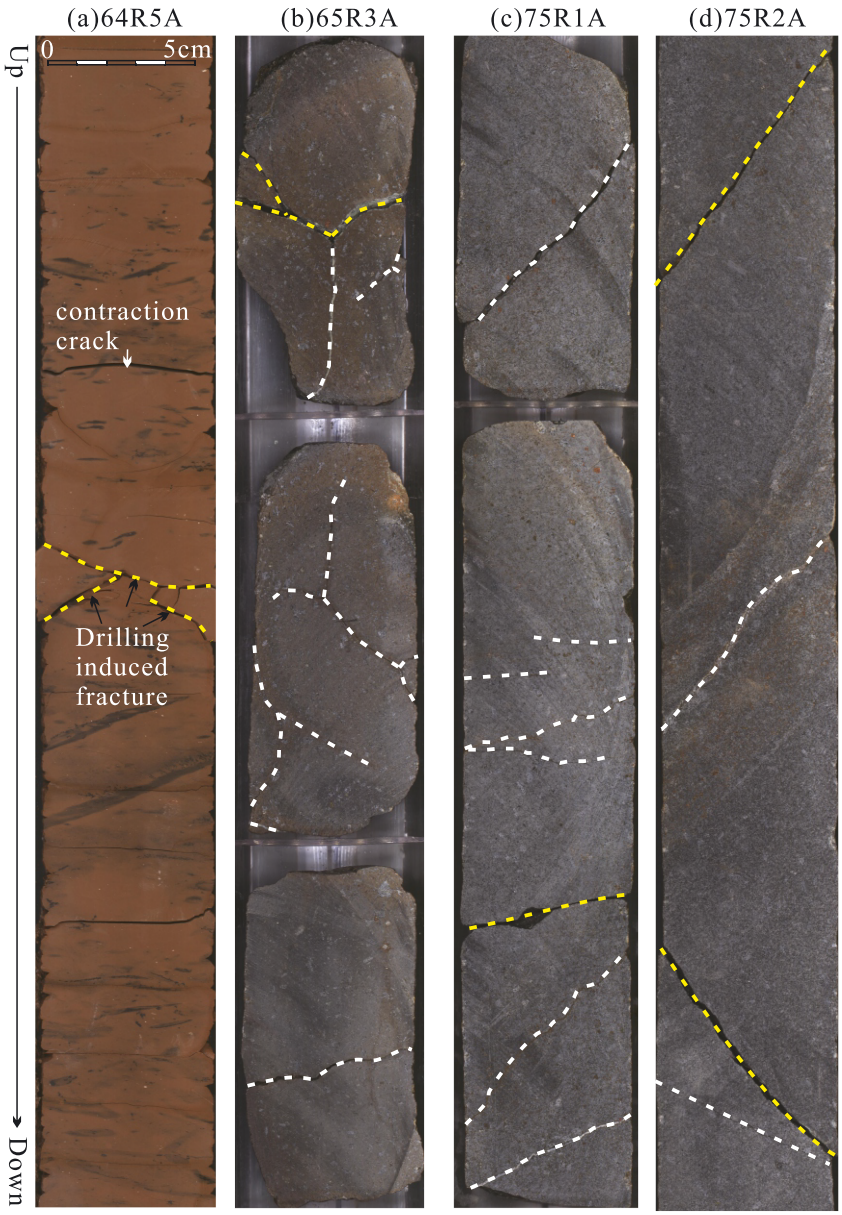

Figure 9. Interpretation on core samples to indicate the fractures and veins at Site U1433. (a) In the intermediate consolidated sediment, no typical fractures were revealed; only layer-parallel contraction cracks were seen; (b) in pillow basalt, curved or triple-juncture fractures and veins were seen; (c, d) in massive flow basalt, straight fractures or veins can be seen. Either curved or straight fractures or veins are fewer than that of Site U1431. White dashed lines are veins or sequence boundaries between layers with different dipping angles. Yellow dashed lines are fractures.

Basalt at Site U1433 was less fractured than that of U1431 (Li, Lin, et al., 2015), so that more fractures can be measured and counted due to the cores' continuity (Figures 9c and 9d). Structures at Site U1433 show clear preference for roughly NS (N350–360°), NE (N50–60°), and EW (N80–90°) orientations (Figure 8b1) and a weak NW (N310–320°) tendency. Dip angles varied over a broad range from nearly horizontal to vertical (Figure 8c3). Most NE and nearly EW trending faults have dip angles smaller than 60° (Figure 8b2), but most NS and NW trending faults show high angles of 60–90°, suggesting that they might be transform faults.

5. Discussion

The orientation distribution of macrostructures at both Sites U1431 and U1433 show two or more preferential orientations, which suggests that their formation may have been affected by multitectonic events

with different stress fields. The potential factors include postspreading and synspreading tectonic events. In order to clarify the relationship between structures and different tectonic events, we discriminate the relict spreading ridge and fracture zone first, constrained with the different kinds of geophysical data including bathymetry, gravity, magnetic, and ocean bottom seismometer (OBS) velocity. Then, we will confirm the postspreading tectonic activity in the SCS after ~15 Ma, considering that it may affect or destroy structures or deformations formed during the earlier synspreading stage. Then we identify the synspreading structures and spreading directions. Finally, we check the latest spreading history in this area.

5.1. Geophysical Data Analysis for the Relict Ridge and Fracture Zone

Controversy in the relict ridge location (Barckhausen et al., 2014; Briais et al., 1993; Li et al., 2014; Sibuet et al., 2016; Taylor & Hayes, 1980; Zhao et al., 2018) prevents the recognization of spreading scenarios. Recent OBS surveys revealed a low *P* wave velocity zone in the upper crust across the rift valley of the SWRR (Zhang et al., 2016) and the seamount chain of the East Subbasin (He et al., 2016; white circles in Figures 3, 4, and 11). Previous studies have found that relict ridges typically exhibit low velocities in the upper crust because of the existence of extrusive high-porosity rocks, volcaniclastic sediments, and shallow faults (Grevemeyer et al., 2001; Weigel & Grevemeyer, 1999). The NE trending relict ridge proposed by Sibuet et al. (2016) and Zhao et al. (2018) is not consistent with the detected low *P* wave velocity zone.

To further constrain the position of the relict ridge, new marine gravity anomaly (Figure 3) and magnetic anomaly data (Figure 4) were examined. The SWRR is very clear on the FAA map, showing a negative anomaly in a positive background. The range of the SWRR on FAA map is consistent with the low velocity zone in the upper crust (Zhang et al., 2016). However, the ERR is not easily discerned due to strong postspreading volcanism. On the magnetic anomaly map, both the SWRR and ERR are very clear, especially the ERR. Along the seamount chain, there is a wide negative magnetic anomaly zone (Figure 4). A similar negative magnetic anomaly was also observed in the SWRR, but much narrower. Within this negative anomaly zone, several nearly EW trending positive anomalies could be identified (Figure 10). Similar EW trending positive reversals were also seen in the SWRR. The negative magnetic anomaly zone agrees very well with the low *P* wave velocity zone (Figure 4). This negative anomaly zone extends westward to 160°E (Figure 4b) and connects with the SWRR through the roughly NS trending ZFZ.

These features combined to suggest that the ERR may most possibly follow the seamount chain and that the NS trending ZFZ may have acted as the transform fault when the East and SW subbasins spread.

5.2. Seamounts, Slickensides, and Postspreading Tectonic Event

Over 20 seamounts were found in the SCS basin. Geochemical analysis and radioactive dating suggest that most of these seamounts are composed of ocean island basalt and erupted after seafloor spreading at the age of 3 to 15 Ma (Figure 1) (Li et al., 1991; Tu et al., 1992; Wang et al., 2009; Yan et al., 2008; Yang et al., 2011; Zhong et al., 2018). The linear axes of the seamounts trend mainly NE and WNW; they should be formed in similar stress field (Figures 11a and 11b). Orientation distribution rosette map shows that they have a first-order long axis trending WNW (N290–300°) and nearly EW (N90–100°). A few of them trend NE to ENE (Figure 11c). Orientations such as NW and nearly NS were also reported on some seamounts close to the transition zone between the East and SW Subbasins (Zhao et al., 2018). It has been suggested that the long duration and large amounts of postspreading active magmatism along or near the SCS spreading ridge may be related to the arrival of the Philippine Sea Plate after the middle Miocene and the subduction of SCS oceanic crust and/or the upwelling of the Hainan plume (Fan et al., 2017; Yu et al., 2018; Zhang et al., 2017). Seamounts developed mainly along the relict ridges and the fracture zones, where thin lithosphere might be easier for magma to break through. More seamounts occurring close to the Manila trench seem to support the hypothesis that subduction of SCS oceanic crust may contribute to the eruption of postspreading magmatism; the bending of subducting SCS plate may cause extension and magma eruption. Although the chemical composition in U1431 and U1433 basalt all indicate fertile mantle upwelling (Yu et al., 2018; Zhang et al., 2017), no ridge-plume interaction was observed.

Same as seamounts, the preferential orientation of planes with slickensides in consolidated sediment will reflect only postspreading tectonic stress field because they were mainly measured on cores younger than

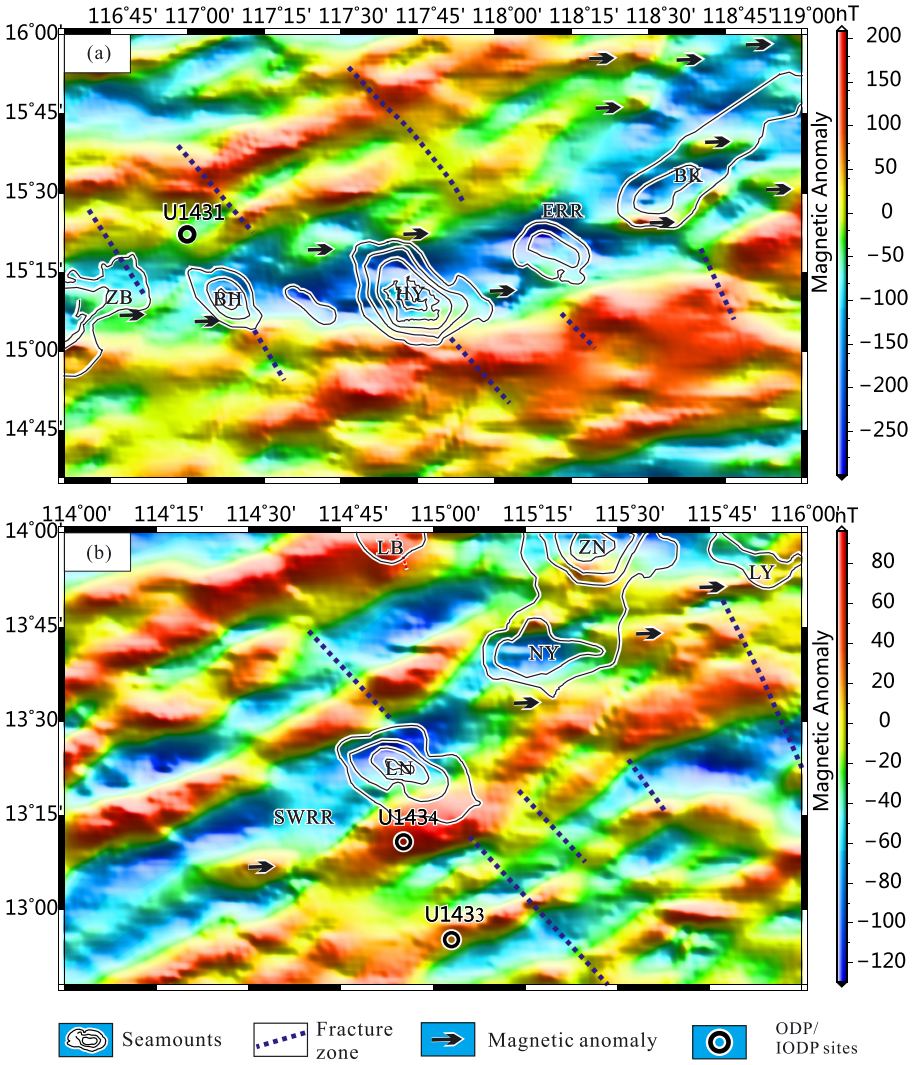

Figure 10. The zoom-in total field magnetic anomaly for the central relict ridge area of the East (a) and SW (b) Sub-South China Sea basin. The positions of the two zoom-in boxes are shown in Figure 4a. In order to observe the relationship between magnetic anomaly lineation and the postspreading volcanism, contour lines of seamounts were projected. Several nearly EW trending positive reversals (black arrows with white background) are indicated along the relict ridge, which show no relationship to postspreading volcanism. Blue dashed lines are conjectured fracture zones interpreted based on bathymetry (Figure 1) and free air gravity (Figure 3) map. Seamounts are drawn mainly according to topography data; some of them as Zhenbei (ZB), Huangyan (HY), Longnan (LN), Nanyue (NY), and Zhongnan (ZN) are confirmed by dredging (Li et al., 1991; Tu et al., 1992; Wang et al., 2009; Yan et al., 2008; Yang et al., 2011).

13 Ma at Site U1431 (36 R and above, Li, Lin, et al., 2015). The strong tendencies of WNW (N300–310°) and nearly EW trending (N80–90°) structural planes in consolidated sediment are consistent with the linear axes orientations of the postspreading seamounts (Figures 8 and 11), which confirmed the existence of postspreading tectonic event. Considering that the NW trending fracture zone near Site U1431 appears transpressive in seismic profiles (Figures 5a and 5a′), which is consistent with the regional earthquake focal mechanism, we conjecture that the postspreading stress may mainly originate from the obduction of the Philippine Sea Plate. GPS measurements suggest that the Luzon Arc moves at a rate of 81–86 mm/year toward the SCS in a direction of roughly N300° (Yu & Kuo, 1999). This direction is consistent with the stress field analysis in the northern continental margin during the last 16 Myr (Li et al., 1989; Sun et al., 2014; Xie et al., 2017). According to the stress ellipse analysis, the WNW and nearly EW trending structures may represent tensional (N) and transtensional shear (R) faults (Figure 11d). They may control the eruption of postspreading volcanism.

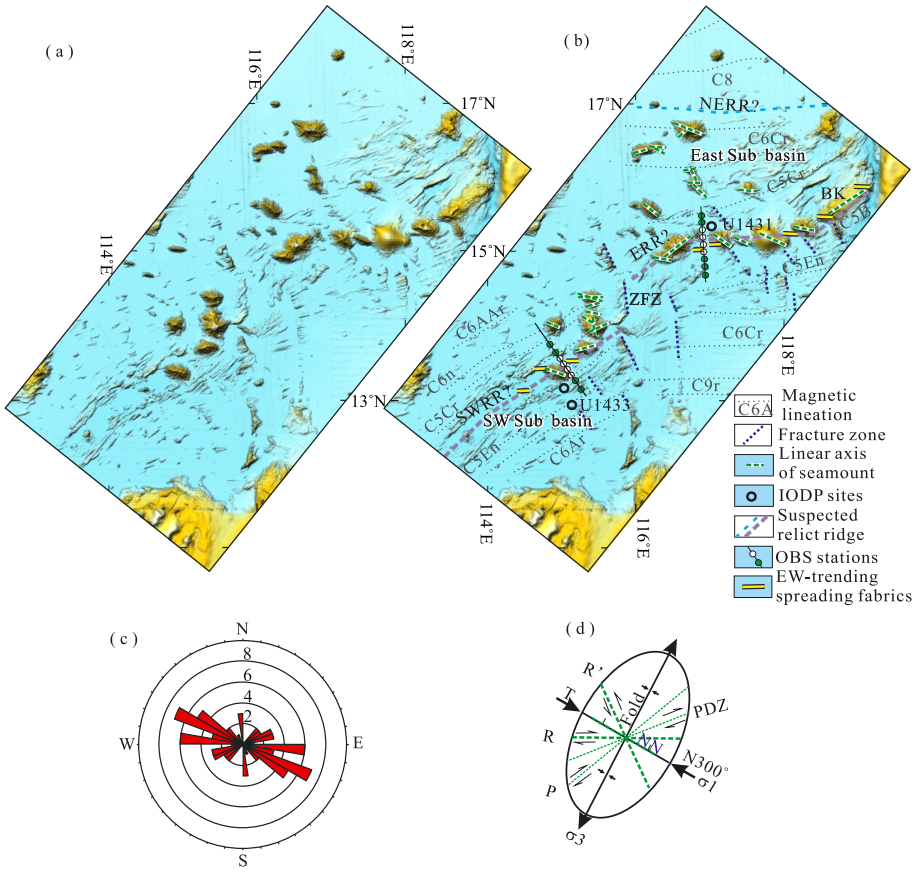

Figure 11. The original (a) and interpreted (b) high-resolution bathymetry map for the relict ridge, orientation distribution of the ridge axes for seamounts (c), and planes with slickensides in sediments at Site U1431 as well as the formation stress field analysis (d). The magnetic lineation is according to Li et al. (2014). The OBS lines are referenced from He et al. (2016) and Zhang et al. (2016). Low *P* wave velocity was detected in the upper crust below the white balls but not below the green balls. Most of the seamounts have a first-order long axis trending either WNW (N290–300°) or nearly EW (N80–90°); few of them trend NE to ENE. The long axes of the seamounts are also indicated with green dashed lines in Figure 4. The long-axis orientations of the postspreading seamounts are consistent with orientations of structural planes in consolidated sediment cores, which suggests that their formation may be controlled by the same stress field. IODP = Integrated Ocean Drilling Program; OBS = ocean bottom seismometer.

5.3. Macrostructures in Basalt and the Spreading Direction

The fractures and veins in the basalt of both sites suggest two similar overwhelming orientations of NS and NE, which are very different from those of the postspreading sediments. Especially for Site U1433, almost none structure was observed in the postspreading sediment sample and very few in the neighbor area along seismic profile (Figures 5b and 5b′). This suggests that the large number of structures in basalt might be formed during seafloor spreading stage, especially the dominating NS and NE trending structures. According to the seismic profiles, most faults in the basalt of U1431 cut through Tg boundary and extend upward into the sediments in short distances. These seismic observations are consistent with the orientation measurements from core samples. Structures at Site U1431 show combined features of both synspreading and postspreading. So in addition to NE (N50–60°) and NS trending (N350–360°) structures, WNW trending (N290–300°) and nearly EW (N90–100°) structures are also observed in a certain amount (Figure 8).

NE and NS trending structures are not typical extensional and transform fault pair under the same spreading direction. Rosette maps suggest that there are also two other directional structures, the steep (dip angle of 60–90°) NW trending (N320–330°) (Figures 8a3 and 8b3) and the normal to steep (wide range of dip angle from 0 to 90°) EW trending structures (Figures 8a2, 8b2, and 8b3). These two directions are perpendicular to the

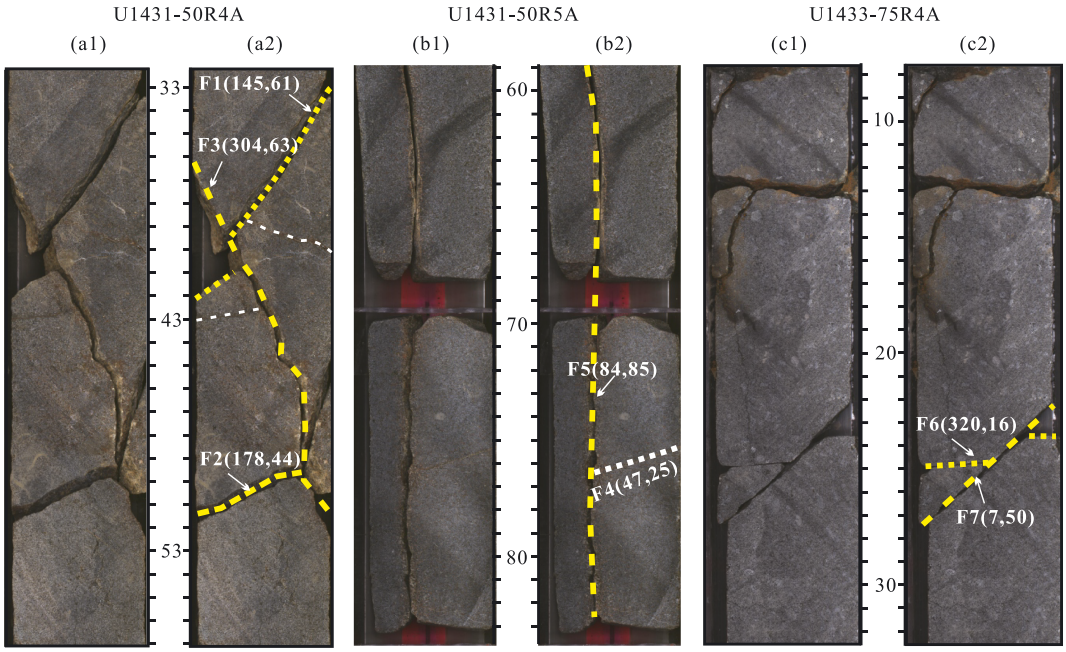

Figure 12. The crosscutting relationship between the structures with different orientations. At Site U1431, the WNW trending structure F3 (strike N304°, dip angle 63°) cuts through the NW trending F1 (strike N145°, dip angle 61°) and the nearly NS trending F2 (strike N178°, dip angle 44°) structure (a1, a2); the nearly NS trending F5 fault (strike N84°, dip angle 85°) cuts through the NE trending F4 fault (strike N47°, dip angle 25°; b1, b2). At Site U1433 (c1, c2), a nearly NS trending structure F7 (strike N7°, dip angle 50°) crosscuts the NW trending (strike N320°, dip angle 16°) fracture. If the above crosscutting relationships represent the order of different episodes of deformation, it suggests that the SE spreading (NW and NE trending structures formed) of the South China Sea occurred first, followed by roughly NS spreading (EW and NS trending structures) and then by WNW compression (WNW trending structures formed).

dominating NE and NS directions. NE and NW trending structures constitute an extensional and transform fault pair; their prevailing occurrence in the lower basalt layer than the upper one (Figures 8b1 and 8b2) may suggest that they were formed earlier than the NS and EW trending structure pair.

In order to determine the order of different tectonic events, crosscutting relationship between different oriented structures were analyzed (Figure 12). At Site U1431, the WNW trending structures in Core 50R4A cut through both the NW trending F1 and the nearly NS trending F2 faults (Figures 12a1 and 12a2). In Core 50R5A, the nearly NS trending F5 fault cuts through the NE trending F4 fault (Figures 12b1 and 12b2). At Site U1433 (Figures 12c1 and 12c2), similar crosscutting relationship was observed. The nearly NS trending structure F7 crosscuts the NW trending fracture F6. The above relationship may suggest that the NE and NW oriented synspreading structure pair occurred earlier than the NS oriented synspreading structures, and the NS trending synspreading structure formed earlier than the postspreading WNW trending structures.

5.4. Conclusive Model and Uncertainties

Integrated with macrostructure and geophysical data analysis, we propose that after the SE-directional spreading at about 20–16 Ma (Barckhausen et al., 2014; Briais et al., 1993; Li et al., 2014; Taylor et al., 1980; Figure 13a), SCS might have experienced another short stage of spreading (Figure 13b). The nearly EW trending normal reversals inside the negative magnetic anomaly zone, the few EW trending faults inside the relict ridge, and the NS trending ZFZ transform fault, joint with EW trending and NS trending macrostructure pair in the samples, suggest that the last stage of seafloor spreading should be in NS direction. According to the magnetic reversal feature and geochemical dating, the wide negative reversal might correspond to C5br (~16 Ma), and the internal narrow positive reversal might be C5bn (~15 Ma). So this NS oriented spreading event lasted for about 1 Ma. This age duration is consistent with the microfossil and basalt dating (Li, Lin, et al., 2015; Koppers, 2014).

Later the WNW compression from the Philippine Sea Plate caused the formation of WNW trending and nearly EW trending structures (Figure 13c). Postspreading volcanic eruptions occurred in a chain along

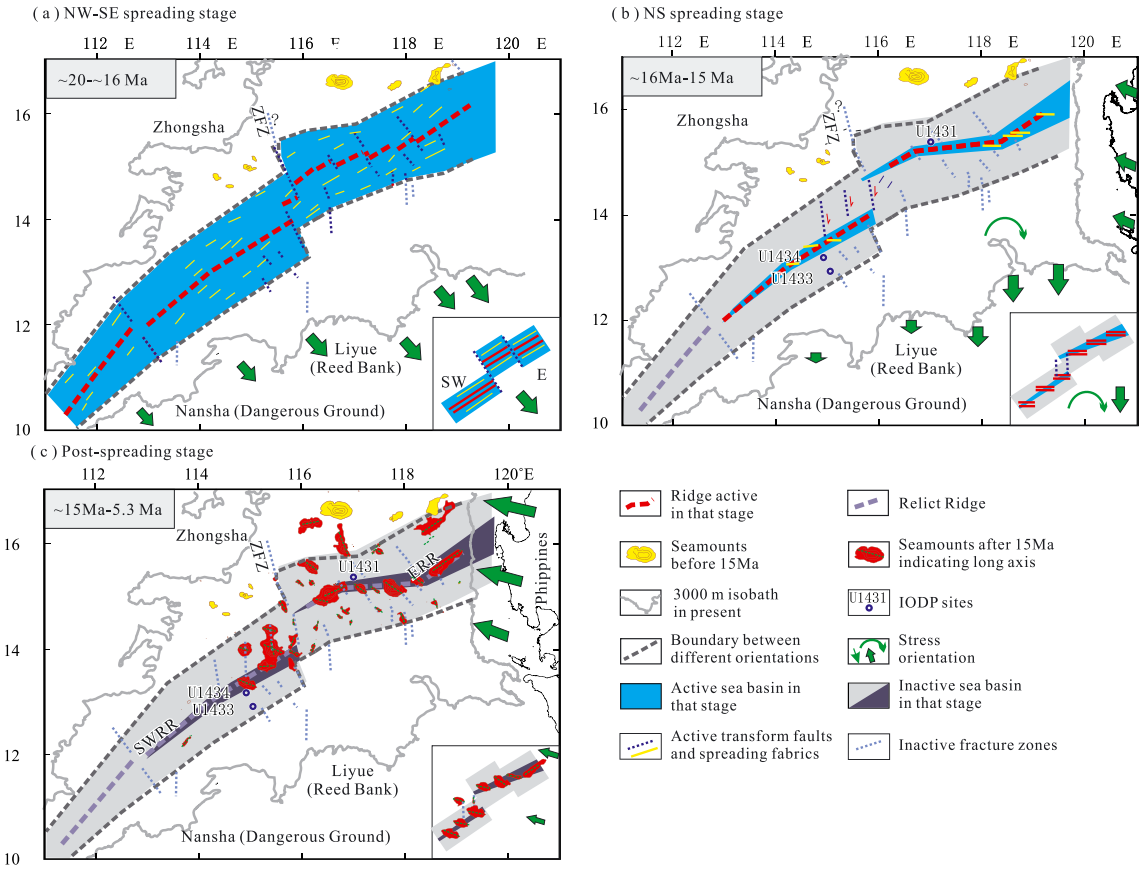

Figure 13. The evolution model of the South China Sea. (a) NW-SE spreading stage in Early–Middle Miocene; (b) NS spreading in Middle Miocene; and (c) WNW compression after Middle Miocene. Sketch figure of each stage was inserted into the lower right corner to show the deformation in a simple way. The age of different stages is mainly referenced to the magnetic lineation and IODP drilling Expedition 349 (Li, Lin, et al., 2015). IODP = Integrated Ocean Drilling Program.

the relict ridges and NS trending fracture zones but with long axes mainly parallel to newly formed transtentional or normal faults. The faster obduction of Philippine Sea Plate in the north than in the south (Yu & Kuo, 1999) may generate differential stress toward the northern and southern slabs of the SCS, which in turn led to regional extension and the eruption of some NE trending seamounts.

This model resolved the inconsistency between the NS trending fracture zones and the SE oriented extension during the latest spreading stage of the SCS. However, there are still some uncertainties, especially for the NS spreading stage, because (1) only limited numbers of EW trending fabrics were discriminated in bathymetry map, and similarly EW trending macrostructures are also less observed. (2) Although NS trending macrostructures were detected in core samples, no NS trending transform faults close to the drill site or along the relict ridge were observed other than ZFZ.

Lacking NS trending transform fault along the relict ridge can be explained as not enough age offset due to transient spreading. According to Hosford and Lin's (2002) research on fast- to ultraslow-spreading ridges, discontinuities with age offsets greater than 2–3 Myr correspond to stable transform faults, while discontinuities with smaller age contrasts constitute unstable nontransform discontinuity. The very short NS oriented spreading may not generate large enough age offset along the ERR, so that no NS trending transform faults were observed there. Between ERR and SWRR, the age difference is about 4 Myr (C5b versus C6n), where NS trending ZFZ developed.

Lacking EW trending spreading fabrics as well as NS trending transform faults along the relict ridge may also be attributed to the slow- to ultraslow-spreading rate. According to magnetic anomaly lineation, the full spreading rate of the ERR dropped to about 30 mm/year after 18 Ma (Li et al., 2014).

6. Conclusions

Based on a comprehensive analysis of macrostructures of core samples, bathymetry, marine FAA, magnetic anomalies, and seismic profiles, the main conclusions of this study include the following:

1. Macrostructures were widely observed at Sites U1431 and U1433, and they provide new independent evidence on the tectonic history of the SCS.
2. Strike distribution analysis indicates that veins and fractures in basalt show different dominating orientations from structures in postspreading sediments, suggesting that they may have been caused by different mechanisms.
3. Planes with slickensides in sediments at Site U1431 have dominant WNW (N300–310°), nearly EW (N80–90°), and NNE (N20–30°) orientations, suggesting WNW oriented postspreading compression. This orientation distribution is consistent with the linear axes distribution of the postspreading seamounts, suggesting that the stress field was from the compression of the Philippine Sea Plate.
4. In basalt samples from Sites U1431 and U1433, the fractures and veins all indicate a dominant direction of roughly NS (N350–360°) and NE (N50–60°). Crosscutting relationship suggests that NE trending structures formed first, followed by NS trending and then WNW trending structures.
5. The latest relict ridge in the East Subbasin (the ERR) should coincide with the postspreading seamount chain, along which strong negative magnetic anomalies with nearly EW trending normal reversals were identified. A low *P* wave velocity zone detected in the upper crust by OBS along the seamount chain further supports this hypothesis. The nearly NS trending ZFZ fault connects the two relict ridges in the East and SW Subbasins and is interpreted to be the fracture zone that was active during the last spreading stage.
6. Based on macrostructure and geophysical data analysis, we proposed that SCS experienced a short stage of roughly NS spreading after the SE oriented spreading at early Miocene (~20 to ~16 Ma). According to the magnetic anomaly interpretation and dating of core samples, the latest NS spreading occurred at about 16–15 Ma. Uncertainties lie in the absence of NS trending transform fault along the relict ridge and the limited number of EW trending spreading fabrics. Small age offset and slow to ultraslow spreading rate during the last spreading stage might be responsible for this.
7. The latest spreading controlled the formation of NS trending transform faults and the postspreading volcanic eruptions. Although this tectonic event lasted for a very short period, macrostructures at Site U1431 and U1433 recorded it accurately. These results resolve former inconsistencies between SE spreading direction and NS trending transform fault and reveal for the first time the existence of the last stage NS spreading in this area. This study also shows how the kinematics of basin evolution can be jointly analyzed through macroscale structures and regional geophysical data.

Acknowledgments
We appreciate Anne Replumaz and other anonymous reviewers for the constructive suggestions, which improve this paper to a great extent. This research was supported by Guangdong NSF research team project (2017A030312002), K. C. Wong Education Foundation (GJTD-2018-13), the IODP-China Foundation, the NSFC Projects (91628301, 41376027, 41576070, 41576068, 41430962, 41674069, 91528302, and 20153410), U. S. National Science Foundation through Grant EAR-1250444, the Guangdong Province Foundation (41576068), and the Joint Foundation of the Natural Science Foundation of China (NSFC) and Guangdong Province (U1301233). Fucheng Li is thanked for helping with the earthquake epicenter figure for the study area. All the sample photos can be accessed via web address (http://www.iodp.tamu.edu). The archive halves of samples are kept in the Kochi repository. The paleomag data will be published by Xixi Zhao separately. All the other geophysical data have been published; for example, the multichannel seismic could be referenced to Li et al. (2015a), and the gravity data and magnetic anomaly data are from Sandwell et al. (2014) and Ishihara and Kisimoto (1996).

References

Barckhausen, U., Engels, M., Franke, D., Ladage, S., & Pubellier, M. (2014). Evolution of the South China Sea: Revised ages for breakup and seafloor spreading. *Marine and Petroleum Geology*, *58*, 599–611. https://doi.org/10.1016/j.marpetgeo.2014.02.022

Briais, A., Patriat, P., & Tapponnier, P. (1993). Updated interpretation of magnetic anomalies and seafloor spreading stages in the South China Sea: Implications for the Tertiary tectonics of Southeast Asia. *Journal of Geophysical Research*, *98*, 6299–6328.

Ding, W. W., Franke, D., Li, J. B., & Steuer, S. (2013). Seismic stratigraphy and tectonic structure from a composite multi-channel seismic profile across the entire Dangerous Grounds, South China Sea. *Tectonophysics*, *582*, 162–176.

Ding, W. W., Li, J. B., Clift, P. D., & IODP Expedition 349 Scientists (2016). Spreading dynamics and sedimentary process of the Southwest Sub-basin, South China Sea: Constraints from multi-channel seismic data and IODP Expedition 349. *Journal of Asian Earth Sciences*, *115*, 97–113. https://doi.org/10.1016/j.jseaes.2015.09.013

Dziewonski, A. M., Chou, T.-A., & Woodhouse, J. H. (1981). Determination of earthquake source parameters from waveform data for studies of global and regional seismicity. *Journal of Geophysical Research*, *86*(B4), 2825–2852. https://doi.org/10.1029/JB086iB04p02825

Ekström, G., Nettles, M., & Dziewonski, A. M. (2012). The global CMT project 2004–2010: Centroid-moment tensors for 13,017 earthquakes. *Physics of the Earth and Planetary Interiors*, *200-201*, 1–9. https://doi.org/10.1016/j.pepi.2012.04.002

Fan, C. Y., Xia, S. H., Zhao, F., Sun, J. L., Cao, J. H., Xu, H. L., & Wan, K. Y. (2017). New insights into the magmatism in the northern margin of the South China Sea: Spatial features and volume of intraplate seamounts. *Geochemistry, Geophysics, Geosystems*, *18*, 2216–2239. https://doi.org/10.1002/2016GC006792

Grevemeyer, I., Flueh, E. R., Reichert, C., Bialas, J., Kläschen, D., & Kopp, C. (2001). Crustal architecture and deep structure of the Ninetyeast Ridge hotspot trail from active-source ocean bottom seismology. *Geophysical Journal International*, *144*(2), 414–431. https://doi.org/10.1046/j.0956-540X.2000.01334.x

Harris, R. N., Sakaguchi, A., Petronotis, K., Baxter, A. T., Berg, R., Burkett, A., et al. (2013). Methods. In R. N. Harris, A. Sakaguchi, K. Petronotis, & the Expedition 344 Scientists (Eds.), *Proceedings of the Integrated Ocean Drilling Program*, *344*, 10–13. College Station, TX: Integrated Ocean Drilling Program. https://doi.org/10.2204/iodp.proc.344.102.2013

He, E. Y., Zhao, M. H., Qiu, X. L., Sibuet, J.-C., Wang, J., & Zhang, J. Z. (2016). Crustal structure across the post-spreading magmatic ridge of the East Sub-basin in the South China Sea: Tectonic significance. *Journal of Asian Earth Sciences*, *121*, 139–152. https://doi.org/10.1016/j.jseaes.2016.03.003

Hosford, A., & Lin, J. (2002). Structural evolution from a strike-slip transform fault to a non-transform discontinuity: Examples from 57°–58°30′E on the SW Indian Ridge and geodynamic implications: 2002 AGU Fall Meeting, T52E-04.

Hutchison, C. S. (2014). Marginal basin evolution: The southern South China Sea. *Marine and Petroleum Geology*, *21*, 1129–1148.

Hwang, C., & Chang, E. T. Y. (2014). Seafloor secrets revealed. *Science*, *346*(6205), 32–33. https://doi.org/10.1126/science.1260459

Ishihara, T., & Kisimoto, K. (1996). Magnetic anomaly map of East Asia, scale 1:4.000.000 [CD-ROM]: Geological Survey of Japan and Coordinating Committee for Costal and Offshore Geoscience Programs in East and Southeast Asia, Tokyo, Japan.

Kinoshita, M., Tobin, H., Ashi, J., Kimura, G., Lallemant, S., Screaton, E. J., et al., & the Expedition 314/315/316 Scientists (2009). *Proceedings of the Integrated Ocean Drilling Program*, (Vol. *314/315/316*). Washington, DC: Integrated Ocean Drilling Program Management International, Inc. https://doi.org/10.2204/iodp.proc.314315316.122.2009

Koppers, A. P. (2014). On the $^{40}Ar/^{39}Ar$ dating of low-potassium ocean crust basalt from IODP Expedition 349, South China Sea: 2014 AGU Fall Meeting, T31E-03.

Li, C. F., Li, J. B., Ding, W. W., Franke, D., Yao, Y. J., Shi, H. S., et al. (2015). Seismic stratigraphy of the central South China Sea basin and implications for neotectonics. *Journal of Geophysical Research: Solid Earth*, *120*, 1377–1399. https://doi.org/10.1002/2014JB011686

Li, C.-F., Lin, J., Kulhanek, D. K., & the 349 Scientists (2015). *Proceedings of the International Ocean Discovery Program*, *South China Sea Tectonics*, (Vol. 349). College Station, TX: International Ocean Discovery Program. https://doi.org/10.14379/iodp.proc.349.2015

Li, C.-F., Xu, X., Lin, J., Sun, Z., Yao, Y. J., Zhao, X. X., et al. (2014). Ages and magnetic structures of the South China Sea constrained by deep tow magnetic surveys and IODP Expedition 349. *Geochemistry Geophysics Geosystems*, *15*, 4958–4983. https://doi.org/10.1002/2014GC005567

Li, J. B., Ding, W. W., & Wu, Z. Y. (2012). The propagation of seafloor spreading in the southwestern subbasin, South China Sea. *Chinese Science Bulletin*, *57*(24), 3182–3191. https://doi.org/10.1007/s11434-012-5329-2

Li, P. (1989). Tectonic structures and evolution of the Pearl River Mouth basin. *China Offshore Oil and Gas (Geology)*, *3*, 11–18. (in Chinese)

Li, Z. L., Qiu, Z. L., Qin, S. C., Pang, X. B., Liang, D. H., Teng, Y. Y., & Li, Y. (1991). A study on the forming conditions of basalts in seamounts of the South China Sea. *Acta Mineral Sincia*, *11*, 326–333. (in Chinese with English abstract)

Morley, C. K. (2002). A tectonic model for the Tertiary evolution of strike-slip faults and rift basins in SE Asia. *Tectonophysics*, *347*(4), 189–215. https://doi.org/10.1016/S0040-1951(02)00061-6

Morley, C. K. (2012). Late Cretaceous-early Paleogene tectonic development of SE Asia. *Earth Science Reviews*, *115*(1-2), 37–75. https://doi.org/10.1016/j.earscirev.2012.08.002

Pautot, G., Rangin, C., Briais, A., Tapponnier, P., Beuzart, P., Lericolais, G., et al. (1986). Spreading direction in the central South China Sea. *Nature*, *321*(6066), 150–154. https://doi.org/10.1038/321150a0

Ru, K. (1988). The development of superposed basin in the northern margin of South China Sea and its tectonic significance. *Oil and Gas Geology*, *9*, 12–18.

Sandwell, D. T., Muller, R. D., Smith, W. H. F., Garcia, E., & Francis, R. (2014). New global marine gravity model from CryoSat-2 and Jason-1 reveals buried tectonic structure. *Science*, *346*(6205), 65–67. https://doi.org/10.1126/science.1258213

Sibuet, J.-C., Yeh, Y. C., & Lee, C.-S. (2016). Geodynamics of the South China Sea. *Tectonophysics*, *692*, 98–119. https://doi.org/10.1016/j.tecto.2016.02.022

Sun, Z., Xu, Z. Y., Sun, L. T., Pang, X., Yan, C. Z., Li, Y. P., et al. (2014). The mechanism of post-rift fault activities in Baiyun Sag, Pearl River Mouth basin. *Journal of Asian Earth Sciences*, *89*, 76–87.

Sun, Z., Zhao, Z. X., Li, J. B., Zhou, D., & Wang, Z. W. (2011). Tectonic analysis of the breakup and collision unconformities in the Nansha. *Chinese Journal of Geophysics*, *54*(6), 1069–1083. https://doi.org/10.1002/cjg2.1685

Sun, Z., Zhong, Z. H., Keep, M., Zhou, D., Cai, D. S., Li, X. S., et al. (2009). 3D analogue modeling of the South China Sea: A discussion on breakup pattern. *Journal of Asian Earth Sciences*, *34*(4), 544–556. https://doi.org/10.1016/j.jseaes.2008.09.002

Sun, Z., Zhou, D., Zhong, Z. H., Xia, B., Qiu, X. L., Zeng, Z. X., & Jiang, J. Q. (2006). Research on the dynamics of the South China Sea opening: Evidence from analogue modeling. *Science in China, Series D*, *49*, 1053–1069.

Taylor, B., & Hayes, D. E. (1980). The tectonic evolution of the South China Basin. In D. E. Hayes (Ed.), *The tectonic and geologic evolution of Southeast Asian seas and islands*, *Geophysical monograph series*, (Vol. 23, pp. 89–104). Washington, D. C.: American Geophysical Union. https://doi.org/10.1029/GM023p0089

Taylor, B., & Hayes, D. E. (1983). Origin and history of the South China Sea basin. In D. E. Hayes (Ed.), *The tectonic and geologic evolution of Southeast Asian seas and islands (Part 2)*, *Geophysical monograph series*, (Vol. 27, pp. 23–56). Washington, D. C.: American Geophysical Union. https://doi.org/10.1029/GM027p0023

Tu, K., Flower, M. F., Carlson, R. W., Xie, G., Chen, C. Y., & Zhang, M. (1992). Magmatism in the South China basin: 1. Isotopic and trace-element evidence for an endogenous Dupal mantle component. *Chemical Geology*, *97*, 47–63.

Vannucchi, P., Ujiie, K., Stroncik, N., Malinverno, A., & the Expedition 334 Scientists (2012). *Proceedings of the Integrated Ocean Drilling Program*, (Vol. 334). Tokyo: Integrated Ocean Drilling Program Management International, Inc. https://doi.org/10.2204/iodp.proc.334.102.2012

Wang, Y. J., Han, X. Q., Luo, Z. H., Qiu, Z. Y., Ding, W. W., Li, J. B., et al. (2009). Late Miocene magmatism and evolution of Zhenbei-Huangyan seamount in the South China Sea: Evidence from petrochemistry and chronology. *Acta Oceanologica Sinica*, *31*, 93–102.

Watts, A. B. (2001). *Isostasy and flexure of the lithosphere*, (Vol. 303). Cambridge: Cambridge University Press.

Weigel, W., & Grevemeyer, I. (1999). The Great Meteor seamount: Seismic structure of a submerged intraplate volcano. *Journal of Geodynamics*, *28*, 27–40.

Xie, Z. Y., Sun, L. T., Pang, X., Zheng, J. Y., & Sun, Z. (2017). Origin of the Dongsha event in the South China Sea. *Marine Geophysical Research*, *38*(4), 357–371. https://doi.org/10.1007/s11001-017-9321-8

Yan, Q. S., Shi, X. F., Wang, K. S., Bu, W. R., & Xiao, L. (2008). Major element, trace element, Sr, Nd, Pb isotopic studies of Cenozoic basalts from the South China Sea. *Science in China Series D: Earth Sciences*, *51*, 550–566.

Yang, S. Y., Fang, N. Q., Yang, S. X., Yao, B. C., & Liang, D. H. (2011). A further discussion on formation background and tectonic constraints of igneous rocks in central subbasin of the South China Sea. *Earth Science - Journal of China University of Geosciences*, *36*, 455–470.

Yao, B. (1995). Characteristics and tectonic significance of the Zhongnan-Liyue Fault (in Chinese), Memo. 7, pp. 1-14, Geological Research of the South China Sea, Guangzhou, China.

Yao, B. C., Zeng, W. J., Chen, Y., Zhang, X., Hayes, D. E., Diebold, J., et al. (1994). *The geological memoir of South China Sea surveyed jointly by China and USA* (in Chinese), (pp. 1–204). Wuhan, China: China University of Geoscience Press.

Yu, M., Yan, Y., Huang, C. Y., Zhang, X., Tian, Z., Chen, W. H., & Santosh, M. (2018). Opening of the South China Sea and upwelling of the Hainan plume. *Geophysical Research Letters*, *45*, 2600–2609. https://doi.org/10.1002/2017GL076872

Yu, S. B., & Kuo, L. C. (1999). GPS observation of crustal deformation in the Taiwan-Luzon region. *Geophysical Research Letters*, *26*(7), 923–926. https://doi.org/10.1029/1999GL900148

Zhang, G. L., Chen, L. H., Jackson, M. G., & Hofmann, A. W. (2017). Evolution of carbonated melt to alkali basalt in the South China Sea. *Nature Geoscience*, *10*(3), 229–235. https://doi.org/10.1038/ngeo2877

Zhang, J., Li, J. B., Ruan, A. G., Wu, Z. L., Yu, Z. T., Niu, X. W., & Ding, W. W. (2016). The velocity structure of a fossil spreading centre in the Southwest Sub-basin, South China Sea. *Geological Journal*, *51*, 548–561. https://doi.org/10.1002/gj.2778

Zhao, M. H., He, E. Y., Sibuet, J.-C., Sun, L. T., Qiu, X. L., Tan, P. C., & Wang, J. (2018). Post seafloor spreading volcanism in the central east South China Sea and its formation through an extremely thin oceanic crust. *Geochemistry, Geophysics, Geosystems*, *19*, 621–641. https://doi.org/10.1002/2017GC007034

Zhong, L. F., Cai, G. Q., Koppers, A., Xu, Y. G., Xu, H. H., Gao, H. F., & Xia, B. (2018). $^{40}Ar/^{39}Ar$ dating of oceanic plagiogranite: Constraints on the initiation of seafloor spreading in the South China Sea. *Lithos*, *302-303*, 421–426.

Zhou, D., Ru, K., & Chen, H. Z. (1995). Kinematics of Cenozoic extension on the South China Sea continental margin and its implication to the tectonic evolution of the region. *Tectonophysics*, *251*(1-4), 161–177. https://doi.org/10.1016/0040-1951(95)00018-6